

STAR FORMATION IN HIGH-REDSHIFT CLUSTER ELLIPTICALS

CORY R. WAGNER^{1,2}, MARK BRODWIN¹, GREGORY F. SNYDER³, ANTHONY H. GONZALEZ⁴, S. A. STANFORD⁵, STACEY ALBERTS⁶,
ALEXANDRA POPE⁶, DANIEL STERN⁷, GREGORY R. ZEIMANN⁸, RANGA-RAM CHARY⁹, ARJUN DEY¹⁰, PETER R. M. EISENHARDT⁷,
CONOR L. MANCONE⁴, AND JOHN MOUSTAKAS¹¹

Draft version April 3, 2018

ABSTRACT

We measure the star formation rates (SFRs) of massive ($M_* > 10^{10.1} M_\odot$) early-type galaxies (ETGs) in a sample of 11 high-redshift ($1.0 < z < 1.5$) galaxy clusters drawn from the IRAC Shallow Cluster Survey (ISCS). We identify ETGs visually from *Hubble Space Telescope* imaging and select likely cluster members as having either an appropriate spectroscopic redshift or red sequence color. Mid-infrared SFRs are measured using *Spitzer* 24 μm data for isolated cluster galaxies for which contamination by neighbors, and active galactic nuclei, can be ruled out. Cluster ETGs show enhanced specific star formation rates (sSFRs) compared to cluster galaxies in the local Universe, but have sSFRs more than four times lower than that of field ETGs at $1 < z < 1.5$. Relative to the late-type cluster population, isolated ETGs show substantially quenched mean SFRs, yet still contribute 12% of the overall star formation activity measured in $1 < z < 1.5$ clusters. We find that new ETGs are likely being formed in ISCS clusters; the fraction of cluster galaxies identified as ETGs increases from 34% to 56% from $z \sim 1.5 \rightarrow 1.25$. While the fraction of cluster ETGs that are highly star-forming ($\text{SFR} \geq 26 M_\odot \text{yr}^{-1}$) drops from 27% to 10% over the same period, their sSFRs are roughly constant. All these factors taken together suggest that, particularly at $z \gtrsim 1.25$, the events that created these distant cluster ETGs—likely mergers, at least among the most massive—were both recent and gas-rich.

Subject headings: galaxies: clusters: general — galaxies: evolution — galaxies: high-redshift — galaxies: elliptical and lenticular, cD

1. INTRODUCTION

In the local Universe galaxy clusters are primarily populated by quiescent, early-type galaxies (ETGs) with little ongoing star formation and evolved stellar populations (Oemler 1974; Dressler 1980; Caldwell et al. 1993; Gómez et al. 2003; Bressan et al. 2006; Clemens et al. 2009; Edwards & Fadda 2011). Studies of their galaxy populations to $z \lesssim 1$ find that the evolution in the color and scatter of their red-sequences are consistent with simple passive evolution models in which the bulk of their stars formed in a short, high-redshift starburst (Bower et al. 1992; Aragon-Salamanca et al. 1993; Stanford et al. 1998; Kodama 1999; Blakeslee et al. 2006; Mei et al. 2006, 2009; Eisenhardt et al. 2008; Muzzin et al. 2008). However, ΛCDM predicts a more extended, hierarchical formation history. For instance, simulations by De Lucia et al. (2006) find that only $\sim 50\%$ of massive ellip-

tical galaxies would have formed the bulk (80%) of their stellar mass by $z \sim 1.5$. A number of studies in the $z \lesssim 1$ regime have found that the star formation of cluster galaxies increases with redshift (Couch & Sharples 1987; Saintonge et al. 2008; Finn et al. 2008; Webb et al. 2013). Recently, infrared (IR) measurements of the $z > 1$ cluster population have revealed substantial dust-obscured star formation activity (Hilton et al. 2010; Tran et al. 2010; Santos et al. 2013; Brodwin et al. 2013, hereafter B13). Alberts et al. (2014, hereafter A14) found that dust-obscured star formation in cluster galaxies increases with lookback time from $z = 0.3 \rightarrow 1.5$.

Several recent studies of the high-redshift ($z > 1$) cluster population have been conducted using the IRAC Shallow Cluster Survey (ISCS; Eisenhardt et al. 2008). Mancone et al. (2010, 2012) measured the rest-frame near-infrared (NIR) luminosity function evolution, and found that while it matched what would be expected from passive evolution up to $z \sim 1.3$, it disagreed with such a model at $z \gtrsim 1.3$, which they suggested as evidence for a significant epoch of galaxy assembly via merging (see, however, Andreon 2013; Wylezalek et al. 2014). In the hierarchical evolution framework, massive ETGs are formed as the result of major mergers (Negroponte & White 1983; Barnes 1988; Naab & Burkert 2003; Cox et al. 2006), and these mergers can cause bursts of star formation (Sanders et al. 1988; Barnes & Hernquist 1996; Hopkins et al. 2008) and fuel an active galactic nucleus (AGN; Springel et al. 2005) that quenches star formation on the order of a few 100 Myr (Di Matteo et al. 2005; Hopkins et al. 2006). Snyder et al. (2012, hereafter S12) found that red-sequence members have roughly constant stellar ages across $1.0 < z < 1.5$ —indicating that star formation must be ongoing—and bluer and more stochastic colors at $1.0 < z < 1.3$ than would be expected of a passive population. Zeimann et al. (2013), B13, and A14 measured high,

¹ Department of Physics and Astronomy, University of Missouri, 5110 Rockhill Road, Kansas City, MO 64110, USA

² Current Affiliation: Department of Physics, Engineering Physics & Astronomy, Queen’s University, Stirling Hall, Kingston, ON K7L 3N6, Canada; cwagner@astro.queensu.ca

³ Space Telescope Science Institute, 3700 San Martin Drive, Baltimore, MD 21218, USA

⁴ Department of Astronomy, University of Florida, Gainesville, FL 32611, USA

⁵ University of California, Davis, CA 95616, USA

⁶ Department of Astronomy, University of Massachusetts, Amherst, MA 01003, USA

⁷ Jet Propulsion Laboratory, California Institute of Technology, Pasadena, CA 91109, USA

⁸ Department of Astronomy and Astrophysics, Pennsylvania State University, 525 Davey Laboratory, University Park, Pennsylvania 16802, USA

⁹ Spitzer Science Center, MC 220-6, California Institute of Technology, 1200 East California Boulevard, Pasadena, CA 91109, USA

¹⁰ NOAO, 950 North Cherry Avenue, Tucson, AZ 85719, USA

¹¹ Department of Physics and Astronomy, Siena College, 515 Loudon Road, Loudonville, NY 12211, USA

and consistent, $H\alpha$, $24\ \mu\text{m}$, and $250\ \mu\text{m}$ star formation rates (SFRs), respectively, in these clusters.

With these high SFRs, it is clear that members in $1 < z < 1.5$ clusters have not exhausted their supplies of cold gas, which, in combination with the evidence of significant ongoing merger activity, suggests that a substantial number of these mergers are gas-rich. If gas-rich major mergers are common in clusters then the ETGs formed in these mergers would be expected to have high SFRs, at least for a short time after their formation. Conversely, ETGs observed several hundred Myr post-merger would likely appear to be recently quenched.

In this paper we use high-resolution *Hubble Space Telescope* (*HST*) images of ISCS galaxy clusters at $1 < z < 1.5$ to identify isolated, early-type members, and then measure their dust-inferred SFRs using *Spitzer* $24\ \mu\text{m}$ data. The goal of this work is to test whether the high SFRs seen in high-redshift clusters are merely due to the morphological mix—a result of the elevated late-type galaxy (LTG) fraction relative to local clusters—or whether significant star formation is present in the early-types as well.

In §2 we summarize the ISCS cluster sample, multi-wavelength data sets, and red-sequence catalogs of S12 which form the basis of this work. In §3 we describe our criteria for selecting isolated, early-type cluster members, and present our measurements of their star formation activity in §4. We discuss our results in §5 and present our conclusions in §6. Throughout this work, we use AB magnitudes unless otherwise indicated. Stellar masses are estimated using a [Chabrier \(2003\)](#) initial mass function (IMF). We adopt a WMAP7 cosmology ([Komatsu et al. 2011](#)), with $(\Omega_{\Lambda}, \Omega_M, h) = (0.728, 0.272, 0.704)$.

2. DATA

2.1. IRAC Shallow Cluster Survey

The ISCS ([Eisenhardt et al. 2008](#)) identified candidate galaxy clusters in a $7.25\ \text{deg}^2$ area of the Boötes field of the NOAO Deep Wide-Field Survey (NDWFS; [Jannuzi & Dey 1999](#)), over a redshift range of $0.1 < z < 2$, using imaging from the IRAC Shallow Survey (ISS; [Eisenhardt et al. 2004](#)). Using accurate photometric redshifts from [Brodwin et al. \(2006\)](#), a wavelet algorithm was used to identify clusters from the $4.5\ \mu\text{m}$ -selected galaxies as three-dimensional overdensities. The cluster centers were taken to be the peaks in the wavelet detection maps. Three more epochs were subsequently obtained in all IRAC bands as part of the *Spitzer* Deep, Wide-Field Survey (SDWFS; [Ashby et al. 2009](#)), which increased the photometric depth of the IRAC images by a factor of two. The deeper SDWFS data were used to improve the photometric redshift accuracy for all galaxies, as well as to extend the catalog to lower flux limits. The SDWFS catalog is 80% complete at 18.1 mag in the $4.5\ \mu\text{m}$ band ([Ashby et al. 2009](#)).

In this work we focus on 11 spectroscopically confirmed $1 < z < 1.5$ ISCS clusters selected by S12 for follow-up *HST* observations, as described below. We list these clusters, along with their positions and spectroscopic redshifts, in Table 1.

2.2. HST Data

A subset of ISCS clusters spanning $1 < z < 1.5$ were imaged with *HST* in the NIR and optical with instrument and filter combinations chosen to bracket the $4000\ \text{\AA}$ break. NIR data were acquired with the Wide Field Camera 3 (WFC3; [Kimble et al. 2008](#)) at F160W. In the optical, observations were either taken with the Advanced Camera for

TABLE 1
ISCS CLUSTERS

ISCS Cluster Name	R.A. (J2000)	Dec. (J2000)	z_{spec}	N_{ETG}^a	N_{LTG}^b
J1429.2+3357	14:29:15.16	33:57:08.5	1.059	8	5
J1432.4+3332	14:32:29.18	33:32:36.0	1.112	3	4
J1426.1+3403	14:26:09.51	34:03:41.1	1.136	5	7
J1426.5+3339	14:26:30.42	33:39:33.2	1.163	8	5
J1434.5+3427	14:34:30.44	34:27:12.3	1.238	3	4
J1429.3+3437	14:29:18.51	34:37:25.8	1.262	6	3
J1432.6+3436	14:32:38.38	34:36:49.0	1.349	3	4
J1433.8+3325	14:33:51.13	33:25:51.1	1.369	5	7
J1434.7+3519	14:34:46.33	35:19:33.5	1.372	2	7
J1438.1+3414	14:38:08.71	34:14:19.2	1.414	4	9
J1432.4+3250	14:32:24.16	32:50:03.7	1.487	4	6
Total Number				51	61

Notes.

^aNumber of visually selected ETGs

^bNumber of visually selected LTGs

Surveys (ACS; [Ford et al. 1998](#)) in filters F775W, F814W or F850LP, or with the Wide Field Planetary Camera 2 (WFPC2; [Holtzman et al. 1995](#)) at F814W. The reader is referred to S12 for a more detailed description of these data.

We use the all-*HST* color-magnitude relations (CMRs) of 11 distant, spectroscopically confirmed ISCS clusters presented in S12. That work isolated the CMRs by subtracting a passively evolving Coma CMR model with a fixed rest-frame slope. Galaxies brighter than an evolving magnitude limit of $H^*(z) + 1.5$ with color offsets, Δ , within $-0.25 < \Delta < 0.75$ of the model CMR were identified as red-sequence galaxies. To reduce the effect of outliers, they removed galaxies that were more than two median absolute deviations in color from their measured Δ zero point.

We independently calculate the F160W completeness via Monte Carlo methods. We insert 100 artificial stars into each WFC3 cluster image in steps of 0.05 magnitudes from 23 to 25.5, ensuring a minimum separation of 5 pixels between input stars. We repeat this procedure 10 times providing 1000 input sources per magnitude bin, per cluster. We run SEXTRACTOR (ver. 2.8.6, [Bertin & Arnouts 1996](#)) on each image to generate source positions and MAG AUTO magnitudes. We match the SEXTRACTOR positions with our input positions in each magnitude bin, counting the source as matched if it lies within 2 pixels of the input position of the artificial star. For each matched source, we calculate the magnitude difference between the input source and MAG AUTO output, and find that the absolute mean Δmag is $\lesssim 0.2$ up to a magnitude of 24.9. We perform a least squares fit to the fraction of matched sources and find a 90% completeness limit of 24.1 mag, consistent with that found in S12. We confirm that all galaxies in our final cluster sample (§3) have an F160W magnitude brighter than our 90% completeness.

2.3. Mid-Infrared Data

The high-redshift clusters studied in this work were also imaged at $24\ \mu\text{m}$ with the Multiband Imaging Photometer for *Spitzer* (MIPS; [Rieke et al. 2004](#)). The exposure times, which increased with redshift from 12 to 48 min, were designed to produce similar sensitivities in IR luminosity for all clusters. Following the method of [Magnelli et al. \(2009\)](#), MIPS source catalogs were generated by using the positions of objects in the higher-resolution IRAC images as priors. This method produces $24\ \mu\text{m}$ flux measurements (or limits) for all IRAC galaxies. For consistency with B13, we infer

total IR luminosities for these sources using templates from [Chary & Elbaz \(2001\)](#), and convert these to SFRs using the [Murphy et al. \(2011\)](#) relation. The 1σ depth of our SFRs is $\sim 13 M_{\odot} \text{ yr}^{-1}$.

While the [Chary & Elbaz \(2001\)](#) templates typically overestimate L_{IR} at $z > 1.5$ by a factor of $\sim 2\text{--}8$ ([Murphy et al. 2009](#); [Nordon et al. 2010](#); [Rodighiero et al. 2010](#)), it provides an estimate that is accurate to 40% up to $z \sim 1.5$ ([Marcillac et al. 2006](#); [Murphy et al. 2009](#); [Elbaz et al. 2010](#)).

In determining their total L_{IR} to SFR calibration, [Murphy et al. \(2011\)](#) assumed that the entire Balmer continuum is absorbed and reradiated by optically thin dust. They also assumed a solar metallicity, and continuous star formation over a timescale of ~ 100 Myr. The relation was defined using a [Kroupa \(2001\)](#) IMF, which has a similar normalization to the [Chabrier \(2003\)](#) IMF we use to calculate our stellar masses.

2.4. Chandra X-ray Data

[Murray et al. \(2005\)](#) obtained X-ray imaging of the NDWFS field with *Chandra* to depths of 5–15 ks. Follow-up Cycle 10 *Chandra* observations brought the exposure time to a uniform depth of 40 ks for the clusters in the present sample.

2.5. Comparison Field Sample Data

We select our comparison sample of field galaxies from UltraVISTA ([McCracken et al. 2012](#); [Muzzin et al. 2013](#)), a deep K_s -selected survey covering 1.62 deg^2 of the COSMOS field ([Scoville et al. 2007](#)). The publicly available UltraVISTA survey¹² has photometry for $\sim 260,000$ sources in 30 bands, including *Spitzer* photometry in the $24 \mu\text{m}$ band of MIPS and all four channels of IRAC ([Muzzin et al. 2013](#)).

We prune the catalog of stellar objects, contamination from bright stars, and contamination from nearby saturated objects, and select only galaxies brighter than the UltraVISTA 90% completeness limit of $K_{s,\text{tot}} = 23.4$.

[Muzzin et al. \(2013\)](#) estimated stellar masses by using FAST ([Kriek et al. 2009](#)) to fit galaxy spectral energy distributions (SEDs) to template SEDs. The templates were generated with [Bruzual & Charlot \(2003\)](#) models, using a [Chabrier \(2003\)](#) IMF. Photometric redshifts in UltraVISTA were derived by [Muzzin et al. \(2013\)](#) using EAZY ([Brammer et al. 2008](#)). A small subset of our final sample ($N = 6$) has spectroscopic redshifts from the zCOSMOS surveys ([Lilly et al. 2007, 2009](#)).

Following the method in §2.3, we infer total IR luminosities for UltraVISTA galaxies using the [Chary & Elbaz \(2001\)](#) templates, and calculate SFRs with the [Murphy et al. \(2011\)](#) relation.

3. GALAXY SELECTION METHOD

We first build our cluster member sample by selecting galaxies that are robust spectroscopic or red-sequence members (§3.1). We remove galaxies that likely harbor AGNs (§3.2), and galaxies that fall below our uniform stellar mass cut (§3.3). We then describe our selection of a comparison sample of high-redshift field galaxies in §3.4. In order to robustly measure SFRs for cluster members, we select galaxies that are free from potential $24 \mu\text{m}$ contamination due to nearby neighbors, based on visual inspection of optical and IR

images (§3.5.1). We then visually classify our isolated cluster members, separating them into ETGs and LTGs (§3.5.2).

3.1. Identification of Cluster Members

We select the 996 galaxies from the 11 high-redshift ISCS clusters studied in S12 for which we have optical/NIR (*HST*) and $24 \mu\text{m}$ (*Spitzer*) images. We match these galaxies to the 8683 sources in the IRAC $4.5 \mu\text{m}$ -selected SDWFS catalog, choosing galaxies where the separation between the *Spitzer* and *HST* positions is $\leq 2''$. This leaves 505 position matched galaxies with *HST* imaging, and SFR and stellar mass estimates.

SDWFS is effectively a mass-selected catalog, and a portion of the 491 *HST*-detected galaxies that are not matched in SDWFS fall below the uniform IRAC-based stellar mass cut we impose below. The remainder of the unmatched S12 catalog members are likely in close proximity—at least in projection—to some of the matched galaxies. However, in §3.5.1, we remove such non-isolated galaxies. Our F160W images cover roughly the central $2' \times 2'$ of the $\sim 10' \times 10'$ IRAC $4.5 \mu\text{m}$ SDWFS images. As such, the vast majority of the 8178 unmatched SDWFS sources lie outside of the *HST* images. However, we estimate that a few hundred of these unmatched galaxies are undetected in F160W.

To identify the subset of galaxies that are robust cluster members, we only retain for the final catalog objects with either high-quality spectroscopic redshifts consistent with membership ([Eisenhardt et al. 2008](#); B13; [Zeimann et al. 2013](#)), or those that are red-sequence members based on *HST* photometry, as described in §2.2. We cut 231 non-members, reducing our sample to 274 galaxies.

Galaxies that are heavily star-forming might exhibit colors outside the range expected of a galaxy on the red sequence. If such galaxies are indeed members, but also lack spectroscopic redshifts, then they will be excluded from our sample. As such, our analysis yields a lower bound on the total SFR. To assess the impact of this effect, we consider our spectroscopic completeness.

We find that of the 505 position matched galaxies identified above, 252 are classified as non-members through S12's red-sequence analysis. Of these, 43 (17%) have high-quality spectra. However, this does not include 71 galaxies that also have high-quality spectroscopic redshifts, yet were confirmed as non-members, and not included in S12's analysis. Hence, we do not have color information for them, nor are they part of the position matched subset. They do, however, still provide an upper limit of 35% (114/323) to the spectroscopic completeness of galaxies that would be excluded based on their colors.

We further consider morphology¹³, and find that both ETG and LTG red-sequence non-members have spectroscopic completeness of 17% when excluding the spectroscopically confirmed non-members. If we include these galaxies, both morphologies have an upper limit of 30% completeness. The range of possible completeness is fairly low, yet the same for both morphologies. We may indeed be excluding a substantial number of galaxies, and while LTGs are the likeliest candidates for the extreme SFRs mentioned above, they are not likely preferentially excluded.

3.2. Rejection of AGNs

¹² http://www.strw.leidenuniv.nl/galaxyevolution/Ultravista/Ultravista/Data_Products_Download.html

¹³ We note that our use of morphology in this section is based on the classifications we discuss in §3.5.2.

The presence of an AGN can affect the MIR flux, potentially leading to an incorrect estimate of the SFR. While only 1% of local cluster galaxies show AGN signatures (Dressler et al. 1985), the surface density of AGNs increases with redshift (Galametz et al. 2009; Martini et al. 2013), making the effect more prominent in our redshift range of interest.

Following B13, we remove AGNs identified via either X-ray or mid-IR techniques. Galaxies whose counterparts in our 40 ks *Chandra* images were point sources with hard X-ray luminosities brighter than $L_{X,H} > 10^{43}$ erg s⁻¹ were removed as likely AGN. Similarly, objects with signal-to-noise (S/N) ≥ 5 in all IRAC bands that fall in the AGN wedge from Stern et al. (2005), which are reddened in the mid-IR due to heating of their dust by AGN, were also removed. These cuts removed a total 12 objects ($\sim 4\%$ of cluster members), bringing our sample to 262 position-matched cluster members apparently free of significant AGN contamination. The resulting SFRs will necessarily be lower limits due to these exclusions.

3.3. Stellar Masses and Mass Limit

We measure stellar masses for our galaxies using the Bayesian SED fitting code, *iSEDfit* (Moustakas et al. 2013), which infers galaxies’ physical properties by fitting population synthesis models to their broadband SEDs. In this work, we use population synthesis models from Bruzual & Charlot (2003), which are based on the Padova 1994 stellar evolutionary tracks (Girardi et al. 1996), the STELIB empirical stellar library (Le Borgne et al. 2003), and the Chabrier (2003) IMF.

While all of the cluster members, and indeed all the galaxies from our initial sample, are brighter than our 90% F160W completeness limit of 24.1 mag, we impose the 80% IRAC-based completeness limit from B13. We remove the four galaxies that fall below this limit, resulting in 258 cluster members with $\log(M_*/M_\odot) > 10.1$.

3.4. Comparison Field Sample Selection

To match the redshift range of our cluster sample, we select field sources between $1 < z < 1.5$, based on the best redshift available. While Muzzin et al. (2013) reduced the effects of blending in their 24 μ m photometry, to be consistent with our isolated criterion for cluster galaxies, we select only isolated field objects by removing photometric catalog members with a neighbor within 6". We also exclude likely AGNs using IRAC photometry to identify sources that fall into the Stern et al. (2005) wedge. We impose on our field sample the same 80% IRAC-based completeness limit of $\log(M_*/M_\odot) > 10.1$ that we use on our cluster galaxies. With these cuts, our final field sample consists of 1127 isolated galaxies.

We use the updated, higher-redshift version of the morphological catalog of Cassata et al. (2007)¹⁴ to separate ETGs and LTGs. They used a non-parametric automatic technique to classify galaxies, based on the method of Cassata et al. (2005), who used concentration, asymmetry, and clumpiness parameters (Conselice 2003; Abraham et al. 2003; Lotz et al. 2004). Cassata et al. (2007) then extended this to include Gini, and M_{20} , two concentration parameters.

While Cassata et al. (2007) used an automatic technique to separate galaxies, their classifications separate early- and late-type galaxies, matching that of our classifications, which we will discuss below in §3.5.2. With the Cassata et al. (2007)

classifications, our final sample contains 72 ETGs and 1055 LTGs.

3.5. Visual Inspection

3.5.1. Isolation

Because of its broad point spread function ($\sim 6''$, Rieke et al. 2004), a single source in the 24 μ m band of MIPS can be comprised of multiple distinct physical sources. Due to the difficulty in deconvolving a multiple-object SFR into its constituent SFRs, we choose to limit our work to isolated objects. To that end, we visually inspect 24 μ m *Spitzer* images and the available optical *HST* images of the 258 cluster members, removing from our final sample those for which we are not able to rule out significant contributions to the MIPS flux from other nearby objects. Through these inspections, we further reduce our sample by 146 galaxies, resulting in 112 isolated cluster members.

This cut on isolation removes interacting and merging members, thus likely lowering our total measured SFRs. It was necessary, however, to obtain robust SFR measurements for morphological early-types, a key goal of this work. The significant star formation activity seen amongst the isolated red-sequence galaxies (§4) is therefore a lower limit. We do not attempt to correct the SFR to the total value, but simply note that the sense of the correction—to higher cluster SFRs for both early- and late-type members—serves to strengthen our conclusions.

3.5.2. Morphology

We visually inspect the optical and NIR *HST* images of the 112 isolated galaxies in our sample, classifying those consistent with smooth elliptical and S0 shapes as ETGs. Galaxies which exhibit either late-type signatures, or disturbed or irregular morphologies, are collectively classified as LTGs. By requiring the ETGs to have smooth early-type profiles with no signs of interaction, we are removing from this sample galaxies with merger signatures, which again biases our sample against ETGs with potentially higher SFRs. In Figure 1, we show 5" \times 5" optical (left) and NIR (right) cutouts of isolated cluster galaxies we classify as ETGs of varying SFRs and redshifts. Below each galaxy, we list its name, spectroscopic cluster redshift, SFR, and stellar mass. At these redshifts, 5" corresponds to ~ 41 –43 kpc.

S12 performed visual inspections of their sample using F160W images, assigning morphologies and recording the local environments. Additionally, Sérsic indices (n_s) were measured in the F160W filter for all S12 galaxies using GALFIT (Peng et al. 2010) and GALAPAGOS (Häußler et al. 2011), with ETGs defined as having $n_s > 2.5$. These Sérsic index measurements will be described in more detail by C. Mancione et al. (2014, in preparation).

As a test of the robustness of our visual morphological classifications, we compare with the independent S12 classifications. The primary difference between these two morphological catalogs is that our classification takes advantage of the higher resolution ACS and WFPC2 *HST* images, in addition to using the F160W images. Where the visual morphologies differ, the cause tends to be late-type features (typically disks with spiral structure) that are clearly visible in the high resolution optical images but not apparent at F160W. Overall, we find agreement for 91% of the sample. We also test the Sérsic indices measured from the F160W images, finding that this quantitative measure disagrees with 31% of our visual classi-

¹⁴ Publicly available COSMOS data sets, including the morphological catalog used in this work, are located at <http://irsa.ipac.caltech.edu/data/COSMOS/datasets.html>

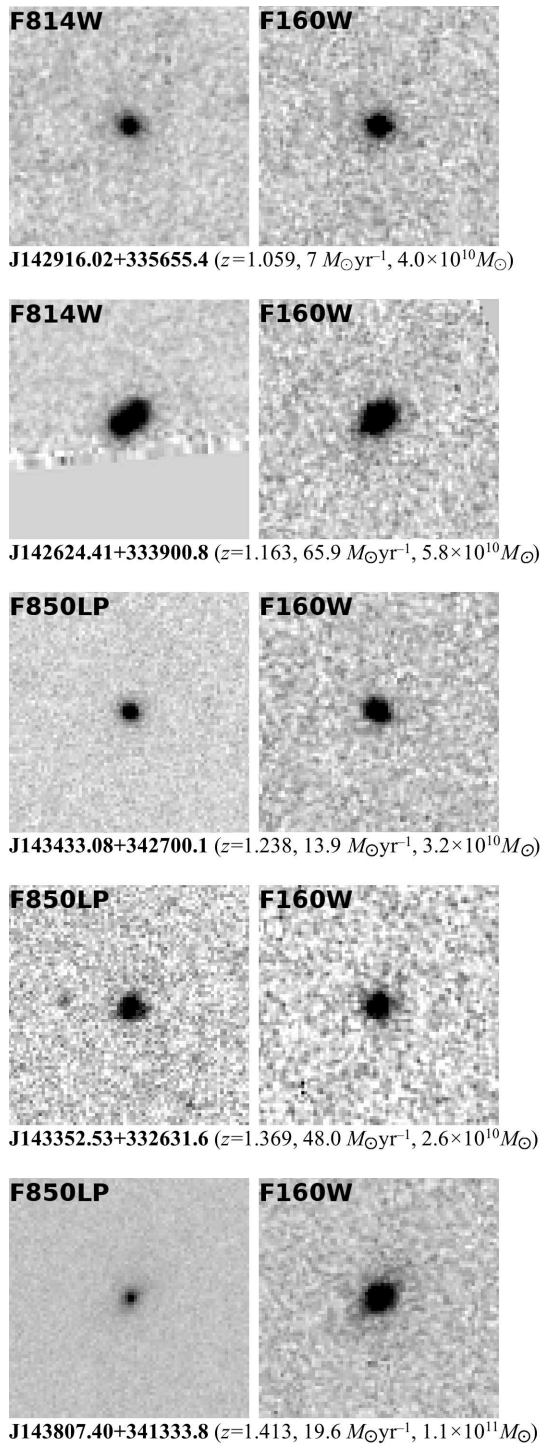


FIG. 1.— $5'' \times 5''$ cutouts of five isolated cluster ETGs, with *HST* filter listed on each image. Listed below each pair of images is the galaxy name, spectroscopic cluster redshift, SFR, and stellar mass.

fications. This high discrepancy level is in line with the 30–40% sample contamination reported by Mei et al. (2012) for selecting morphology using Sérsic indices.

We also test the consistency of using different classification methods for galaxies in clusters and the field by visually classifying a subset of 333 randomly selected UltraVISTA galaxies. We find that our classifications, using COSMOS F814W images, agree for 294 galaxies (88%).

Separating our galaxies into four evenly-sized bins, we plot

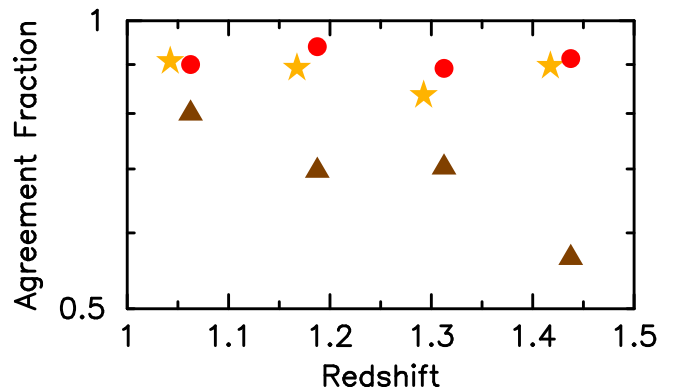


FIG. 2.— Classification agreement for the isolated ISCS cluster sample, between our visual classifications and S12’s F160W-based visual (Sérsic) classifications, shown by the red circles (brown triangles). The agreement between our visual classifications and the Cassata et al. (2007) quantitative classifications for a test set of isolated UltraVISTA field galaxies over $1 < z < 1.5$ is shown by the gold stars. Both the visual/visual cluster agreement, and the visual/quantitative field agreement are high, and show little-to-no redshift dependence. The visual/Sérsic agreement, however, is uniformly lower, and negatively correlated with redshift.

in Figure 2 the visual/visual and visual/Sérsic agreement for cluster galaxies as a function of redshift, as the red circles and brown triangles, respectively. The agreement for the UltraVISTA test set is plotted with the gold stars. The visual/visual agreement for cluster galaxies is high, with no strong redshift dependence. The visual/quantitative agreement for the field sample shows similar results. The cluster visual/Sérsic agreement, however, is uniformly lower, and shows a strong negative trend with increasing redshift.

This low visual/Sérsic agreement is suggestive of potential inaccuracies in the Sérsic classifications, especially at the higher redshifts of our sample. While this could indeed be indicative of inaccuracies in our visual classifications, we expect this is not the case, particularly in light of the uniformly high agreement between our visual classifications and the quantitative Cassata et al. (2007) classifications. With this high and uniform agreement, we conclude that using quantitative classifications for the field sample while using visual classifications, instead of Sérsic, for the cluster sample is appropriate. We have, however, run the analysis both ways and have verified that none of the major qualitative results depend on this choice. Our final sample of visually classified isolated cluster ETGs (LTGs) contains 51 (61) galaxies, and the breakdown by cluster is listed in Table 1.

4. ANALYSIS

4.1. Star Formation Rate vs. Radius

All the isolated galaxies in our sample are robustly detected in optical and IRAC imaging, and our MIPS $24 \mu\text{m}$ fluxes are measured for *all* sources using these positional priors. The resulting SFRs are thus physically meaningful down to very low significances, albeit with large uncertainties.

In the left panel of Figure 3 we plot SFR versus projected clustercentric radius for isolated cluster ETGs (red filled circles) and LTGs (blue open squares). Galaxies plotted below the horizontal dashed line have SFRs below our 1σ depth of $13 M_{\odot} \text{yr}^{-1}$. The large error bar shows the systematic error in the SFR, which we take to be 40%, based on a comparison between $24 \mu\text{m}$ and *Herschel* SFR measurements over $z = 0–1.5$ (Elbaz et al. 2010).

On their own, the ETG and LTG samples show little-to-no radial dependence in the SFRs. However, when considering

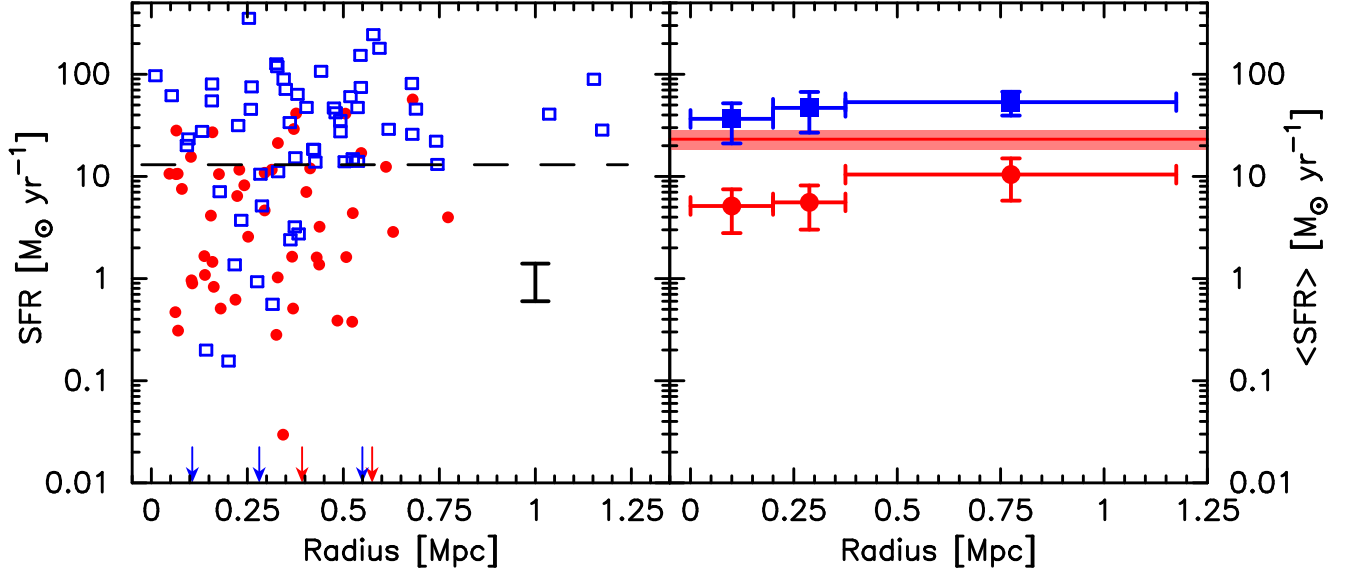


FIG. 3.— *Left panel:* SFR versus clustercentric radius for isolated cluster ETGs (red filled circles), and LTGs (blue open squares). The horizontal dashed line is the 1σ SFR detection level ($13 M_{\odot} \text{ yr}^{-1}$), and the large error bar represents the 40% systematic uncertainty in the SFRs. The arrows indicate the location of cluster members undetected in MIPS (SFR = 0). SFRs of isolated cluster galaxies—of all morphological types—are weakly correlated with projected radius. *Right panel:* Mean SFR versus clustercentric radius for isolated ETGs (red circles) and LTGs (blue squares), with bin widths depicted by the horizontal error bars. In each bin, the median SFR of non-detections is assigned to each undetected galaxy and included in the mean. The vertical error bars show the quadrature sum of bootstrap resampling and Poisson error. The solid horizontal red line (shaded region) is the mean SFR (error) for isolated field ETGs. On average, cluster ETGs are forming stars at 14% the rate of cluster LTGs, and nearly 30% that of field ETGs.

all isolated cluster galaxies, we do find a weak correlation (Spearman’s $r_s = 0.26 \pm 0.06$ at the 99% confidence level) between SFR and clustercentric radius.

As can be seen in the left panel of Figure 3, we are largely limited to radii less than 0.75 Mpc due to the small footprint of WFC3. We are able to probe beyond 1 Mpc in J1432.4+3250 due to two adjacent pointings on this cluster. We have verified our results are unchanged if we limit our analysis to the well-sampled region below 0.75 Mpc.

4.2. Mean Star Formation Rate

To explore the effect of environment on the SFRs of both isolated ETGs and LTGs, we show in the right panel of Figure 3 the mean SFR, $\langle SFR \rangle$, as a function of projected clustercentric radius. ETGs are plotted as red circles and LTGs as blue squares. We separate the galaxies into three non-overlapping annuli, selecting the radial bins such that the S/N in each is approximately equal. From inner to outer, the bin sizes are 200, 175, and 800 kpc, respectively. The errors in each bin are calculated from the quadrature sum of bootstrap resampling (1000 samples, with replacement) and simple Poisson errors. We also show the mean SFR of our comparison sample of isolated field ETGs with the red horizontal line. The 68% error in the mean is given as the shaded region.

In computing the mean SFRs, objects with individual SFRs below $13 M_{\odot} \text{ yr}^{-1}$ were assigned the median value of all such objects in the bin. This is the catalog-space equivalent of median stacking; from inner to outer annuli, the median SFRs of these ETGs (LTGs) are 1.5, 2.6, and 2.2 (0.2, 2.4, and 1.4) $M_{\odot} \text{ yr}^{-1}$. We have verified that none of our main results change even in the extreme case of setting the SFRs of all such $< 1\sigma$ SFRs to zero.

We find mean SFRs of 5 ± 2 , 6 ± 3 , and $10 \pm 5 M_{\odot} \text{ yr}^{-1}$ for our cluster ETG sample from the inner to outer annulus, respectively. With mean SFRs of 40 ± 20 , 50 ± 30 , and $40 \pm 10 M_{\odot} \text{ yr}^{-1}$ over the same range, the LTGs have mean SFRs ~ 5

to 8 times higher at all radii. Both ETGs and LTGs show some decrease in mean SFR at small radii, although this is not statistically significant given the large errors. Averaging over all radii we find a mean SFR of $7 \pm 2 M_{\odot} \text{ yr}^{-1}$ for cluster ETGs, which is a factor of 7 lower than for cluster LTGs ($\langle SFR \rangle = 50 \pm 10 M_{\odot} \text{ yr}^{-1}$). While the uncertainty in our SFRs is too large to determine any radial dependence, we also find that cluster ETGs show suppressed star formation activity relative to field ETGs, which have $\langle SFR \rangle = 23 \pm 5 M_{\odot} \text{ yr}^{-1}$.

These results show that although cluster ETGs have SFRs that are fairly quenched relative to both their field analogs and the remainder of the isolated cluster population, they still contribute 12% of the vigorous star formation observed amongst the isolated galaxies in these clusters.

4.3. Fraction of Star-forming Galaxies

In Figure 4, we plot f_{SF} , the fraction of star-forming isolated cluster ETGs (red circles) as a function of clustercentric radius. We conservatively limit this measurement to members with SFRs of at least $26 M_{\odot} \text{ yr}^{-1}$, above our 2σ detection level. We use only two annuli due to the relatively small size of our sample, and use the binomial error in the fraction as our total error. The radial bins and error ranges are shown by the horizontal and vertical error bars, respectively. The horizontal red line shows the fraction of star-forming isolated field ETGs, with the binomial error in the fraction shown by the shaded region. The gray points and error bars show the fraction of local ($z \lesssim 0.1$) star-forming ($L_{\text{IR}} > 4.7 \times 10^{10} L_{\odot}$) cluster galaxies versus projected radius, from Chung et al. (2011, hereafter C11), who studied 69 low-redshift clusters with total dynamical masses in the range $\sim (1-7) \times 10^{14} M_{\odot}$, determined by using caustic infall patterns (Rines & Diaferio 2006), and selecting only galaxies brighter than $M_r = -20.3$. The lower x-axis corresponds to the projected clustercentric radius for this work, while the upper x-axis corresponds to the projected R_{200} -normalized radius from C11. Based on

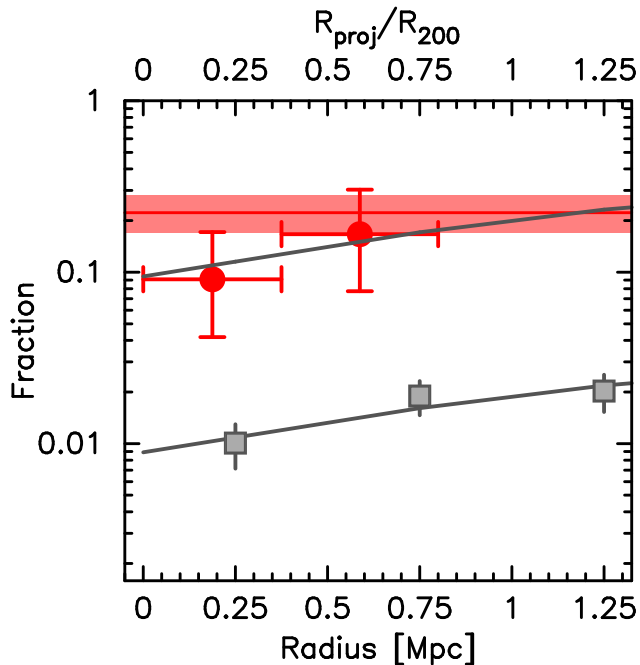


FIG. 4.— Fraction of star-forming galaxies versus projected radius for high-redshift isolated cluster ETGs (red circles) and low-redshift cluster galaxies from C11 (gray squares and error bars). For cluster ETGs, the size of the horizontal error bars represents the bin widths, and the vertical error bars represent the binomial error in our fractions. The lower axis corresponds to the data from this work; the upper from C11. The lower gray curve is a least squares fit to all six points from Figure 4 of C11 (extending to $3R_{\text{proj}}/R_{200}$), while the upper gray curve is the same fit, shifted up by a factor of 10.6. The red horizontal line (shaded region) shows the fraction (error) for the comparison high-redshift isolated field ETGs. High-redshift cluster ETGs have star-forming fractions at least an order of magnitude higher than local cluster galaxies, and two times lower than field ETGs in the same redshift range.

the X-ray, weak lensing and dynamical masses that have been measured for a subset of the Boötes clusters (Brodwin et al. 2011; Jee et al. 2011), as well as on a clustering analysis of the full ISCS sample (Brodwin et al. 2007), our $z > 1$ ISCS clusters have halo masses in the range $\sim(0.8 - 2) \times 10^{14} M_{\odot}$, and virial radii of ~ 1 Mpc. Therefore the upper and lower axes in Figure 4 are approximately equivalent. While the median mass of the C11 clusters is larger than that of the Boötes clusters, the latter will grow in mass in the $\sim 8-9$ Gyr to the present epoch.

Averaging over all radii, we find that $12_{-5}^{+6}\%$ of isolated cluster ETGs are star-forming. It is clear that the star-forming fraction is substantially higher at $z > 1.0$ than it is locally. We quantify this difference by first fitting a least squares curve to all six C11 points (while only the first three points are shown in Fig. 4, the C11 measurements extend to $3R_{\text{proj}}/R_{200}$), then using χ^2 minimization to determine that a simple scaling factor of 10.6 provides an excellent fit to our data. In both radial bins, we find that the fraction of star-forming ETGs in our sample is approximately an order of magnitude higher than for local cluster galaxies of all types.

Due to the very low redshift of the clusters in C11 ($z \lesssim 0.1$), their minimum cutoff for star-forming galaxies ($L_{\text{IR}} > 4.7 \times 10^{10} L_{\odot}$) is ~ 3 times lower than our 2σ level of $\sim 1.5 \times 10^{11} L_{\odot}$. Using the published L_{IR} values from C11, we find that six of the 109 cluster galaxies (within $3R_{\text{proj}}/R_{200}$) considered star-forming in C11 have $L_{\text{IR}} > 1.5 \times 10^{11} L_{\odot}$, which is only $\sim 0.1\%$ of their cluster member sample, a factor of ~ 18 lower than with their SFR cut, and ~ 100 times lower than our

cluster ETG fraction.

Within the errors, we do not have enough evidence to determine whether there is a radial trend in our ETGs, though the shifted radial profile of C11, indicated by the upper curve, is clearly consistent with our data. Also, the f_{SF} of field ETGs ($0.22_{-0.05}^{+0.06}$) is approximately twice that of the overall fraction for cluster ETGs, implying an environmental dependence on isolated ETG star formation.

4.4. Specific Star Formation Rate

We next explore the specific star formation rate (sSFR), defined as the sum of the SFRs divided by the sum of the stellar masses, in each radius bin. In normalizing the SFR of a galaxy to its mass, the sSFR allows us to explore the relative efficiency with which it converts its cold gas into stars.

In Figure 5 we plot the sSFR versus radius for both our cluster ETGs (red circles and error bars) and for the low-redshift, star-forming, cluster galaxies of C11 (gray points). The radial binning and error ranges for our points are calculated as in Figure 3. We show the sSFR and similarly calculated error of field ETGs as the red horizontal line and shaded region, respectively.

As in §4.3, we fit a best-fit curve to the C11 points, then determine the shift in amplitude required to match our cluster ETG points. We find that scaling the curve by a factor of $10^{2.07}$, also shown in the figure, provides a good fit to our high-redshift sSFR measurements. High-redshift cluster ETGs are forming stars at a rate 120 times higher than local cluster galaxies.

C11 calculated sSFR for star-forming ($L_{\text{IR}} > 4.7 \times 10^{10} L_{\odot}$) galaxies, while we place no such constraint on either high-redshift ETG sample plotted in Figure 5. Additionally, the morphological mix of the low redshift cluster galaxies to which we are comparing is unclear. Although clusters in the local Universe are primarily inhabited by early-type, “red and dead” galaxies (Oemler 1974; Dressler 1980), the star-forming subset detected by C11 may be preferentially drawn from the small fraction of late-type members or from recently accreted field galaxies. Correcting for such LTG contamination, and removing the L_{IR} limit, would lower the sSFR in the low redshift sample, and hence make the evolution over this redshift range even more dramatic.

Averaging across all radii, high-redshift cluster ETGs have an sSFR of $0.10 \pm 0.03 \text{ Gyr}^{-1}$, which is a factor of 4 lower than the sSFR of the field ETG sample ($0.4 \pm 0.1 \text{ Gyr}^{-1}$). While we cannot definitively determine whether there is a radial trend in cluster ETG sSFR, this drop relative to ETGs in the field is further evidence for the environmental dependence of the star formation of high-redshift isolated ETGs, as shown in the previous two sections.

What is not immediately clear is how much of this offset between cluster and field ETG sSFR is due to the difference in the distribution of stellar masses and how much is due to star formation activity. If the mass distribution of field and cluster ETGs was identical, we could conclude that the large difference in sSFR between the two samples was due entirely to star formation activity. However, even though the minimum stellar mass allowed in each sample is the same ($1.3 \times 10^{10} M_{\odot}$), the mean mass of cluster ETGs, $7.0 \times 10^{10} M_{\odot}$, is 1.4 times larger than that of field ETGs ($5.2 \times 10^{10} M_{\odot}$). Clearly, the lower sSFR of cluster ETGs must be due, at least in part, to their higher stellar masses. To quantify this impact, we temporarily replace the stellar mass of each field ETG with

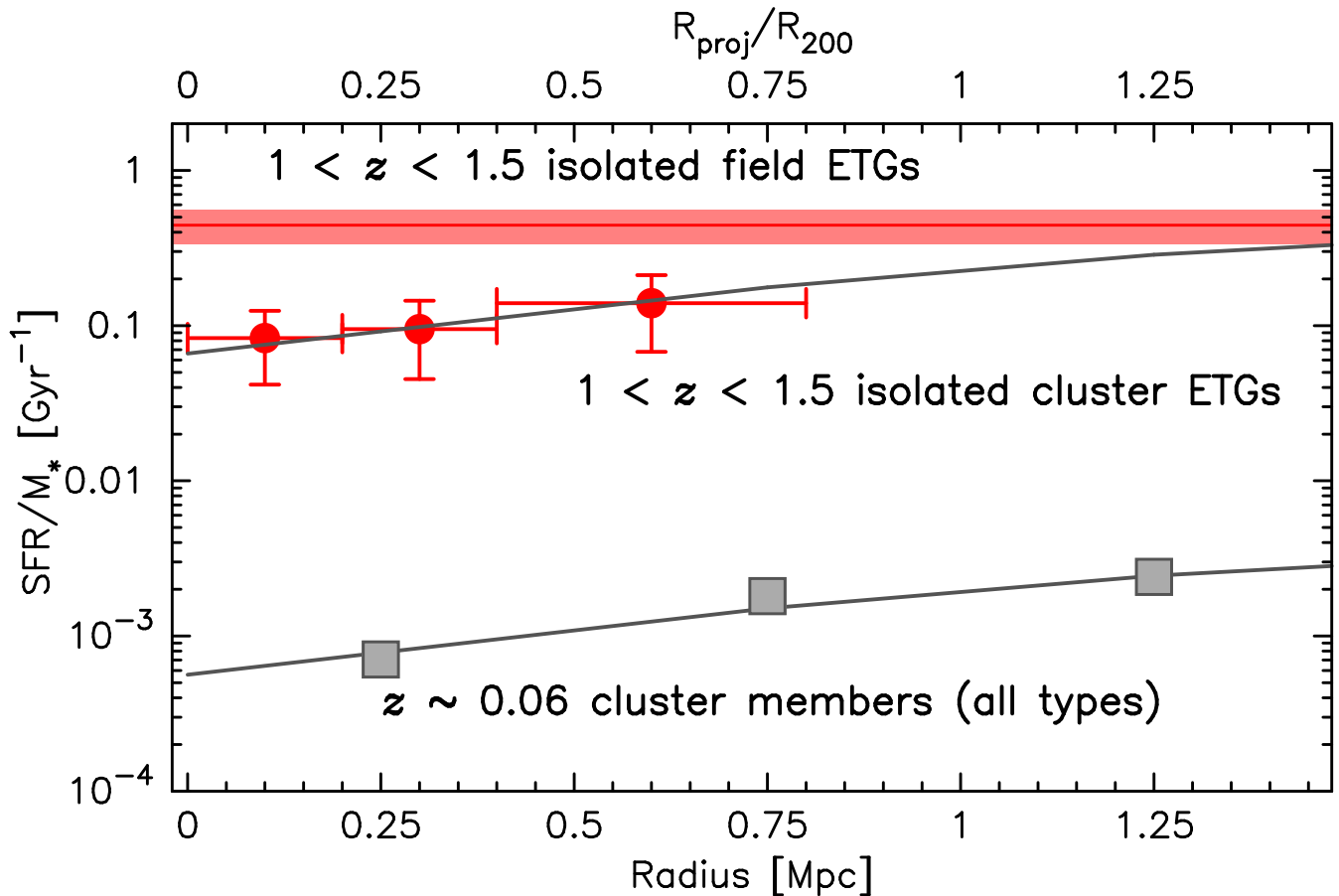


FIG. 5.— Specific SFR versus radius for high-redshift isolated cluster ETGs (red filled circles) and low-redshift cluster galaxies from C11 (gray filled squares), with the same x-axes as Figure 4 (§4.3). The vertical error bars represent the bootstrapping and Poisson error in our sSFRs, and the horizontal error bars show the size of each bin. The lower gray curve is a least squares fit to the C11 points (all six points from their Fig. 3, extending to $3R_{\text{proj}}/R_{200}$), while the upper gray curve is the same fit shifted up by a factor of 120. The red horizontal line (shaded region) shows the sSFR (error) for the comparison high-redshift isolated field ETGs. The sSFR of high-redshift cluster ETGs is four times lower than similar redshift field ETGs, yet more than two orders of magnitude larger than low-redshift cluster galaxies of all types. While we place no lower limit on the L_{IR} of high-redshift cluster ETGs, C11 only measured sSFR for galaxies with $L_{\text{IR}} > 4.7 \times 10^{10} L_{\odot}$ (their star-forming cut; see §4.3). The sSFR of C11’s cluster galaxies would be lower if no cut was imposed, making the factor of 120 we find here a lower limit.

the mean stellar mass of cluster ETGs. The sSFR of field early-types is now 0.3 Gyr^{-1} , still a factor of 3 larger than for cluster ETGs. This value is 75% of the actual field ETG sSFR, which implies that only 25% of the offset is due to ETG stellar masses, and the bulk of the difference is from the field-relative quenching of cluster ETGs.

5. DISCUSSION

5.1. Comparisons with Related ISCS Work

Two related studies (B13, and A14) identified high levels of star formation activity in a superset of the ISCS clusters studied in this work. However, these studies could not isolate the ETGs due to a lack of morphological information. In the present work, which benefits from the high-resolution imaging of *HST*, we are able to expand upon their results by analyzing the star formation properties of isolated, massive ETGs, and comparing them to high-redshift, massive, isolated ETGs in the field and to galaxies in low-redshift clusters.

5.1.1. Comparison to B13

B13 measured the star formation activity in 16 ISCS galaxy clusters at $1.0 < z < 1.5$, including the 11 clusters studied in this work. Their large sample enabled them to finely bin their data as functions of both redshift and radius. The morphology

and isolation cuts in the present work result in a relatively small sample size that precludes a similar analysis, but instead permits an investigation of physically interesting subsamples of these cluster members.

Both B13 and this work used the same $24 \mu\text{m}$ *Spitzer* photometry, so the measurements of star formation activity should be consistent, despite the sample size difference. To test this, we first compared, as a function of redshift, the fraction of isolated star-forming galaxies of *all* types (by combining ETGs and LTGs) from this work to the fraction of star-forming galaxies from B13 within 1 Mpc. We used their redshift binning ($1 < z < 1.2$, $1.2 < z < 1.37$, and $1.37 < z < 1.5$) and adopted their ($S/N \geq 4$) flux limit, corresponding to $\text{SFR} \gtrsim 47 M_{\odot} \text{ yr}^{-1}$. Our results are in good agreement with those reported in B13.

Probing to lower star formation rates, we plot in Figure 6 the fraction of isolated star-forming cluster galaxies down to our full 2σ $\text{SFR} \geq 26 M_{\odot} \text{ yr}^{-1}$ limit. We bin the galaxies ($1 < z < 1.16$, $1.16 < z < 1.35$, and $1.35 < z < 1.5$; shown by the horizontal error bars) such that the binomial error in each redshift bin is approximately equal for galaxies of all morphological type (green filled triangles). ETGs are plotted as red circles and LTGs as blue squares, slightly offset to the left and right, respectively.

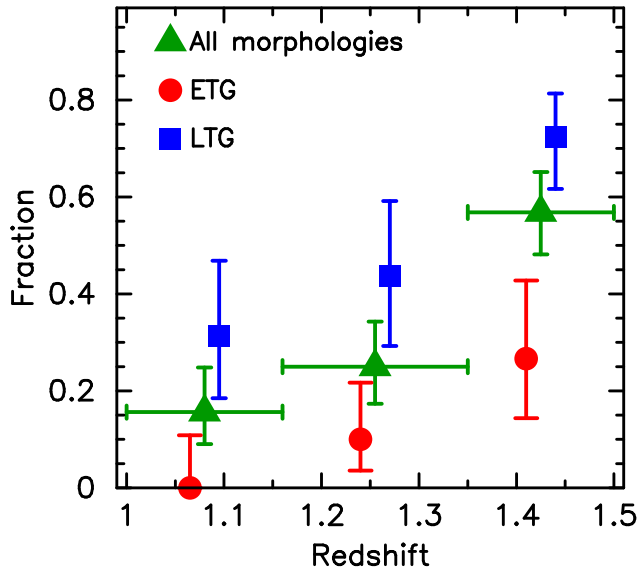


FIG. 6.— Fraction of isolated, high-redshift star-forming ($SFR \geq 26 M_{\odot} \text{ yr}^{-1}$) cluster galaxies (see legend for symbol types) as a function of redshift. Vertical error bars show the binomial error in the fractions, while the horizontal error bars show the redshift binning for all three sets of cluster galaxies. The significant drop in star-forming fraction from 57% to 25% exhibited by all cluster galaxies (green triangles) at $z \sim 1.4$ is in good agreement with the redshift of transition—away from vigorous star formation—observed by B13.

57% of all isolated cluster galaxies of are star-forming at $1.35 < z < 1.5$, followed by a decrease to 25% in the middle redshift bin. This result is in good agreement with the transition redshift of $z \sim 1.4$ found by B13 between the era of vigorous star formation in high-redshift clusters and the quenched epoch at later times. The LTG population experiences a similar trend, with a decrease from 72% to 44%, over the same range, while the ETG sample shows a milder downward trend in star-forming fraction at $z \sim 1.4$ (from 27% to 10%), though it’s formally consistent with being constant within the errors.

5.1.2. Comparison to A14

A14 explored 274 ISCS clusters from $z = 0.3$ to 1.5, including ~ 100 over the same redshift range as our observations. By stacking $250 \mu\text{m}$ *Herschel* data, they were able to probe to mean L_{IR} values almost an order of magnitude lower than our 1σ detection limit. Although our sample is a subset of the A14 sample, the measurement techniques— $24 \mu\text{m}$ detections versus stacking at $250 \mu\text{m}$ —are relatively independent. Here we compare some of our results with those reported in A14.

In order to compare the two SFR measurements for our morphologically selected sample, we first attempted to directly measure stacked $250 \mu\text{m}$ fluxes for our ETG and LTG samples. However, with the relatively small sample size, and source contamination due to the large beam size ($18''$, Swinyard et al. 2010), the S/N was too low to permit this measurement.

In Figure 7 we compare mean SFR as a function of redshift, derived from $24 \mu\text{m}$ and $250 \mu\text{m}$ measurements. To be consistent with the radial selection in A14, we only plot galaxies with clustercentric radii < 1 Mpc. We plot our isolated cluster galaxies as the filled points, using the same binning as in Figure 6. The filled green triangles represent galaxies of all morphologies, while the open triangles show the mean SFR of galaxies of all types from A14. Despite the order of magnitude difference in observed wavelength, and the very differ-

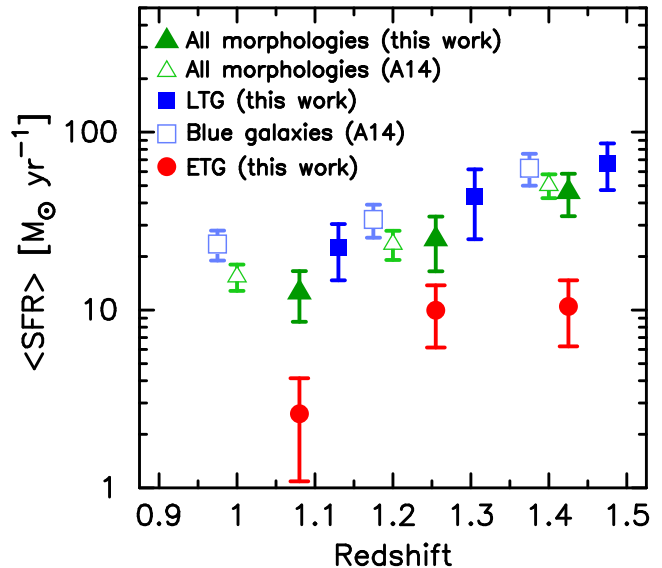


FIG. 7.— Mean SFR versus redshift for our isolated cluster galaxies (filled symbols, with the same binning as in Figure 6) and for cluster galaxies from A14 (open symbols), with all galaxies having clustercentric radius < 1 Mpc. Our errors are calculated as the quadrature sum of bootstrapping and simple Poisson errors. The two different measurement methods used for calculating these SFRs— $24 \mu\text{m}$ detections versus stacking at $250 \mu\text{m}$ —show consistent results.

ent measurement methodologies, the results are in excellent agreement for galaxies of all morphological types.

While unable to visually or quantitatively determine morphologies, A14 matched each galaxy in their sample against seven Polletta et al. (2007) templates representing different morphologies. Using this template fitting as a proxy for color, A14 selected galaxies that were best fit by late-type templates as “blue” (star-forming) galaxies. We plot the mean SFR of these galaxies as the light blue open squares, and compare them to our isolated cluster LTGs (blue filled squares). We again find that there is excellent agreement between the $250 \mu\text{m}$ -derived SFRs in A14 and the $24 \mu\text{m}$ -derived SFRs in this work.

Recent work suggests that SFRs based on MIR observations may be overestimated for galaxies with evolved stellar populations. For example, thermally pulsing asymptotic giant branch C stars may emit up to half their light in the MIR (Kelson & Holden 2010). Utomo et al. (2014) suggest, for MIPS SFRs, up to a two order of magnitude overestimation of the star formation of high L_{IR} galaxies with evolved stellar populations.

The A14 results are based on $250 \mu\text{m}$ *Herschel* stacking, which primarily probes the cold dust regime, and are largely immune to the effects of evolved stellar populations that typically impact MIR wavelengths. If our ETG SFRs were being overestimated to the extent suggested by Utomo et al. (2014), one would expect that the star formation of our *entire* sample would be overestimated, since ETGs make up approximately half of cluster galaxies. If this was the case, the mean SFR of *all* isolated cluster galaxies in Figure 7 would likely be higher than the mean SFR from A14. Due to the consistency between our results and those of A14 for galaxies of all morphologies, we surmise that our early-type population is not strongly impacted by this effect.

5.2. Star Formation in High-Redshift Cluster ETGs

Low-redshift ETGs, particularly those in clusters, have quiescent, old stellar populations. A key issue in the evolution of galaxy populations in clusters is determining the nature of the star formation history of these “red-and-dead” galaxies. Specifically, when did present-day massive cluster ETGs experience their last major burst of star formation? Determining the epoch during which these galaxies experienced such a burst can provide constraints on when cluster galaxies experienced their last phase of gas-rich major merging.

We find that the fraction of star-forming galaxies is an order of magnitude larger for our $1 < z < 1.5$ cluster ETGs than for local cluster galaxies of *all* morphologies (C11). Measurements of star-forming fractions in nearby clusters, such as those by C11, necessarily include large contributions from late-type galaxies as ETGs typically have SFRs below the survey limits. The increase we find is therefore a lower limit to the evolution between nearby and $z > 1$ cluster ETGs.

Even more striking is the comparison of the mass-normalized star formation rates between these two galaxy populations. With sSFRs more than two orders of magnitude higher than cluster galaxies in the local universe, our high-redshift cluster ETGs have significantly more ongoing star formation activity per unit stellar mass. This dramatic evolution would be even more extreme if C11 had measured the sSFRs of all galaxies above a fixed mass limit, rather than just those above their star formation detection limit.

An interesting result stemming from the comparisons in §5.1 is that despite the decline in the fraction of star-forming ($\text{SFR} \geq 26 M_{\odot} \text{ yr}^{-1}$) cluster ETGs at $z \sim 1.4$ seen in Figure 6, this population has mean SFRs that are roughly constant across this period. Specifically, although we see that the star-forming fraction drops ~ 17 percentage points (albeit with very large scatter) at this redshift, their mean SFRs (shown in Figure 7) remain relatively constant from $z \sim 1.4 \rightarrow 1.25$. One potential conclusion from this is that while a significant quantity of early-type galaxies are being quenched, there must be some mechanism that is *enhancing* the star formation activity of the remaining star-forming ETGs.

If the above results are not a product of environment, we would expect to see ETGs in both the cluster *and* the field have a similar lack of SFR evolution. To determine whether this is the case, we plot in the upper panel of Figure 8 the sSFR for cluster and field galaxies, using the redshift binning from Figures 6 and 7. As we are primarily concerned with potential evolution around $z \sim 1.4$, we focus on the two higher redshift bins, shading over the lowest bin. We plot cluster and field ETGs with the filled red and open pink circles, respectively. Field LTGs are represented by the open blue squares. Errors are from the quadrature sum of bootstrap resampling and simple Poisson errors.

The sSFR of cluster ETGs is approximately the same in the two highest redshift bins. Given the large uncertainties, though, we can make no conclusions on whether a trend exists. However, we do find that relative to field galaxies, the sSFR of cluster ETGs shows a weak—or perhaps even no—dependence on redshift from the highest to the middle redshift bin. This evidence suggests that any potential enhancement of cluster ETG star formation may be environmentally dependent.

In the lower panel of Figure 8 we plot the fraction of isolated cluster galaxies that we classified as ETGs, using the same redshift bins as above. We find that the fraction of ETGs increases from 34% to 56% from $z \sim 1.4 \rightarrow 1.25$, which sug-

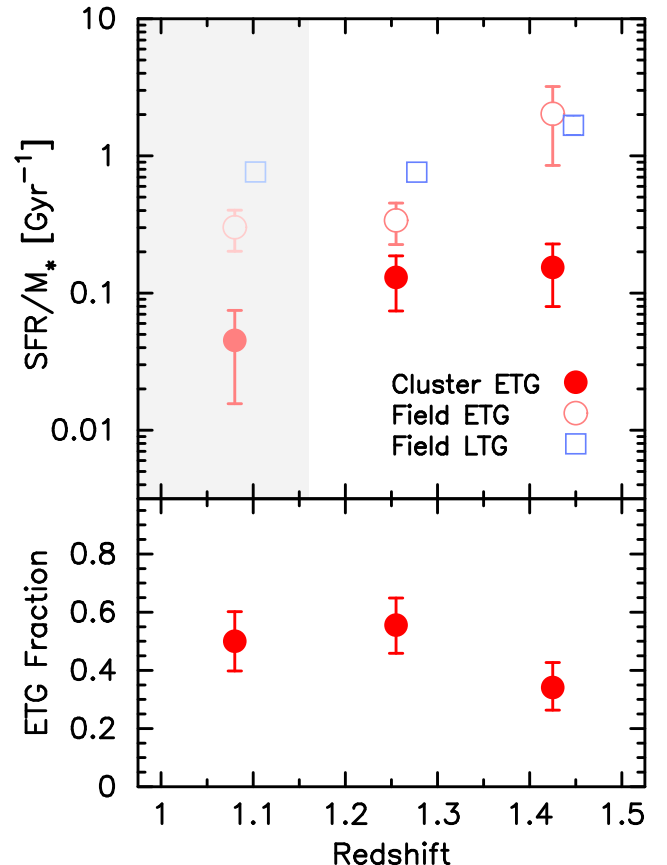


FIG. 8.— *Upper panel:* Specific SFR as a function of redshift for ETGs in clusters (red filled circles) and in the field (pink open circles), and for field LTGs (light blue open squares). Errors are calculated as the quadrature sum of bootstrap resampling and simple Poisson errors, as in §4.4. We shade the lowest redshift bin to guide the eye to two higher bins. Field galaxies show potentially strong sSFR evolution over these two bins around $z \sim 1.4$, while cluster ETGs show little-to-no evolution over the same range. *Lower panel:* Fraction of cluster galaxies that are ETGs as a function of redshift.

gests that new ETGs are being formed during this period.

It should be noted that there are processes other than major merging that may potentially play a role in forming new ETGs, or shaping existing early-types (e.g., Kaviraj et al. 2013). Violent disk instability can cause late-type systems to lose their disks through turbulence, forming compact gas-rich “blue nuggets” with gas inflows similar to those generated by wet mergers (Dekel & Burkert 2014). However, the cold streams (Kereš et al. 2005; Dekel & Birnboim 2006) that feed disks in this model are only important in regions with low galaxy density (Kereš et al. 2005), and likely not a significant factor in the hot halo environment of ISCS clusters.

Strazzullo et al. (2010) found a large fraction of quenched, compact ETGs in the $z = 1.39$ cluster XMMU J2235, suggesting that minor—and likely dry—mergers can increase the size of such galaxies over later epochs, without drastically altering their star formation activity. However, XMMU J2235 is a very massive cluster ($\sim 7 \times 10^{14} M_{\odot}$, Jee et al. 2009; Rosati et al. 2009), where major merger activity has likely ceased, and a factor of at least a few times more massive than the clusters studied in this work. As such, the mechanism suggested by Strazzullo et al. (2010) is not likely *currently* playing a role in ISCS clusters—especially at $z \gtrsim 1.16$ —when considering the star formation activity shown above.

From $z \sim 1.4 \rightarrow 1.25$, the fraction of cluster ETGs that are

star-forming drops from 27% to 10%. It is likely that a substantial number of cluster ETGs formed before $z = 1.5$, and that they make up a significant portion of this large subset of quenched ETGs that we find in ISCS clusters. However, from $1.35 < z < 1.5$ to $1.16 < z < 1.35$, there is a ~ 20 percentage point increase in the fraction of cluster galaxies that are morphologically early-type; some portion of the remaining star-forming ETGs in this epoch are likely recent byproducts of major mergers. Furthermore, cluster ETG mean and specific SFRs are roughly constant over this period. These ETGs have not yet had sufficient time for their star formation to be quenched, implying that their progenitors' mergers occurred relatively recently.

Moving into the lower redshift bin ($1 < z < 1.16$), the star-forming ETG fraction falls to 0%, and their sSFR and mean SFR are both quenched (by factors of 3 and 4, respectively), while the ETG fraction remains relatively constant. Given our assumptions above about gas-rich major mergers, the dearth of star-forming galaxies, and overall lack of star formation activity seen in this epoch, at $1 < z < 1.16$, suggests we are seeing the quenching of ETGs due to post-merger AGN activity.

6. CONCLUSIONS

We have used a sample of 11 high-redshift ($1.0 < z < 1.5$), IR-selected ISCS galaxy clusters to investigate the star formation properties of isolated, early-type galaxies. After conservatively removing AGNs through X-ray and IR criteria, we visually inspected our sample using high-resolution *HST* imaging, separating our galaxy sample into two coarse morphological bins: ETGs and LTGs. We used deep $24 \mu\text{m}$ imaging from *Spitzer* to measure the obscured SFRs, excluding galaxies for which we could not rule out contamination from nearby neighbors.

We compared the star formation of the cluster ETG sample with low-redshift cluster galaxies, finding an order of magnitude larger fraction of star-forming galaxies, and a greater than two order of magnitude larger sSFR for our high-redshift cluster ETGs. Averaging across our entire cluster ETG sample, we find that 12% are still experiencing relatively enhanced ($\text{SFR} > 26 M_{\odot} \text{ yr}^{-1}$) star formation activity.

By comparing the mean SFR of ETGs with LTGs in ISCS clusters, we found that despite their enhanced star formation relative to low-redshift cluster galaxies, high-redshift cluster early-types have substantially less star formation activity relative to the rest of the isolated cluster population. However, averaging across all cluster radii, ETGs still contribute 12% of the significant star formation activity observed in these clusters.

Due to our relatively small sample size, we were unable to detect the radial dependence in star formation activity reported by B13. However, we found that our cluster ETGs are quenched relative to a comparison sample of field ETGs, by a factor of 3 in mean SFR, and 4 in sSFR. Even when ‘‘correcting’’ the sSFR of field ETGs for their factor 1.4 lower mean stellar masses, we find that it only accounts for 25% of the

difference between the field ETG sSFR and the significantly quenched cluster ETG sSFR.

We then used the conservative IR luminosity cut from B13 to compare the fraction of star-forming galaxies, f_{SF} , with their results, finding that our measurements in isolated galaxies agreed with the B13 measurements of all cluster galaxies in these $z > 1$ clusters. We also found that our mean SFR measurements correlated well with those of A14, who measured SFR using stacked $250 \mu\text{m}$ *Herschel* flux.

We used our 2σ SFR detection limit ($26 M_{\odot} \text{ yr}^{-1}$) to explore the f_{SF} evolution from $z \sim 1.5 \rightarrow 1.0$. We considered cluster galaxies of all morphologies and found that while 57% are star-forming at $z \gtrsim 1.4$, the fraction drops to 25% by $z \sim 1.25$. This drop of more than 30 percentage points suggests that the epoch of enhanced star formation in these clusters is ending around $z \sim 1.4$, a finding consistent with that first reported by B13.

While the fraction of star-forming ETGs drops from 27% at $z \sim 1.4$ to 10% by $z \sim 1.25$, their mean and specific SFRs are largely unchanged over this period. With a corresponding increase of ~ 20 percentage points in the fraction of galaxies classified as early-type, these results are consistent with a scenario where major gas-rich mergers form new early-type galaxies, temporarily enhancing their star formation activity.

A number of recent studies of the ISCS cluster population have presented lines of evidence supporting the role of mergers in building the stellar mass in these clusters. Specifically, the NIR luminosity function evolution disagrees with a passive evolution model at $z \gtrsim 1.3$ (Mancone et al. 2010, 2012), galaxies are experiencing substantial star formation (A14, B13, Zeimann et al. 2013), young galaxies are continuously migrating on the cluster red sequence (S12), and an increase in AGN activity has been observed (Galametz et al. 2009; Martini et al. 2013). This work helps to solidify the implications of these studies by demonstrating the redshift dependence of the star formation rate and ETG fraction that are consistent with the picture where massive ETGs are formed in gas-rich major mergers.

This work is based in part on observations made with the *Spitzer Space Telescope*, which is operated by the Jet Propulsion Laboratory, California Institute of Technology under a contract with NASA. Support for this work was provided by NASA through an award issued by JPL/Caltech. Support for *HST* programs 10496, 11002, 11597, and 11663 were provided by NASA through a grant from the Space Telescope Science Institute, which is operated by the Association of Universities for Research in Astronomy, Inc., under NASA contract NAS 5-26555. This work is based in part on observations obtained with the *Chandra X-ray Observatory*, under contract SV4-74018, A31 with the Smithsonian Astrophysical Observatory which operates the *Chandra X-ray Observatory* for NASA.

We thank S. Chung for providing her data in digital form. We also appreciate the UltraVISTA and COSMOS collaborations making their data publicly available.

REFERENCES

- Abraham, R. G., van den Bergh, S., & Nair, P. 2003, *ApJ*, 588, 218
 Alberts, S., Pope, A., Brodwin, M., et al. 2014, *MNRAS*, 437, 437
 Andreon, S. 2013, *A&A*, 554, A79
 Aragon-Salamanca, A., Ellis, R. S., Couch, W. J., & Carter, D. 1993, *MNRAS*, 262, 764
 Ashby, M. L. N., Stern, D., Brodwin, M., et al. 2009, *ApJ*, 701, 428
 Barnes, J. E. 1988, *ApJ*, 331, 699
 Barnes, J. E., & Hernquist, L. 1996, *ApJ*, 471, 115
 Bertin, E., & Arnouts, S. 1996, *A&AS*, 117, 393
 Blakeslee, J. P., Holden, B. P., Franx, M., et al. 2006, *ApJ*, 644, 30
 Bower, R. G., Lucey, J. R., & Ellis, R. S. 1992, *MNRAS*, 254, 601
 Brammer, G. B., van Dokkum, P. G., & Coppi, P. 2008, *ApJ*, 686, 1503

- Bressan, A., Panuzzo, P., Buson, L., et al. 2006, *ApJ*, 639, L55
- Brodwin, M., Gonzalez, A. H., Moustakas, L. A., et al. 2007, *ApJ*, 671, L93
- Brodwin, M., Brown, M. J. I., Ashby, M. L. N., et al. 2006, *ApJ*, 651, 791
- Brodwin, M., Stern, D., Vikhlinin, A., et al. 2011, *ApJ*, 732, 33
- Brodwin, M., Stanford, S. A., Gonzalez, A. H., et al. 2013, *ApJ*, 779, 138
- Bruzual, G., & Charlot, S. 2003, *MNRAS*, 344, 1000
- Caldwell, N., Rose, J. A., Sharples, R. M., Ellis, R. S., & Bower, R. G. 1993, *AJ*, 106, 473
- Cassata, P., Cimatti, A., Franceschini, A., et al. 2005, *MNRAS*, 357, 903
- Cassata, P., Guzzo, L., Franceschini, A., et al. 2007, *ApJS*, 172, 270
- Chabrier, G. 2003, *PASP*, 115, 763
- Chary, R., & Elbaz, D. 2001, *ApJ*, 556, 562
- Chung, S. M., Eisenhardt, P. R., Gonzalez, A. H., et al. 2011, *ApJ*, 743, 34
- Clemens, M. S., Bressan, A., Panuzzo, P., et al. 2009, *MNRAS*, 392, 982
- Conselice, C. J. 2003, *ApJS*, 147, 1
- Couch, W. J., & Sharples, R. M. 1987, *MNRAS*, 229, 423
- Cox, T. J., Dutta, S. N., Di Matteo, T., et al. 2006, *ApJ*, 650, 791
- De Lucia, G., Springel, V., White, S. D. M., Croton, D., & Kauffmann, G. 2006, *MNRAS*, 366, 499
- Dekel, A., & Birnboim, Y. 2006, *MNRAS*, 368, 2
- Dekel, A., & Burkert, A. 2014, *MNRAS*, 438, 1870
- Di Matteo, T., Springel, V., & Hernquist, L. 2005, *Nature*, 433, 604
- Dressler, A. 1980, *ApJ*, 236, 351
- Dressler, A., Thompson, I. B., & Shectman, S. A. 1985, *ApJ*, 288, 481
- Edwards, L. O. V., & Fadda, D. 2011, *AJ*, 142, 148
- Eisenhardt, P. R., Stern, D., Brodwin, M., et al. 2004, *ApJS*, 154, 48
- Eisenhardt, P. R. M., Brodwin, M., Gonzalez, A. H., et al. 2008, *ApJ*, 684, 905
- Elbaz, D., Hwang, H. S., Magnelli, B., et al. 2010, *A&A*, 518, L29
- Finn, R. A., Balogh, M. L., Zaritsky, D., Miller, C. J., & Nichol, R. C. 2008, *ApJ*, 679, 279
- Ford, H. C., Bartko, F., Bely, P. Y., et al. 1998, in *Society of Photo-Optical Instrumentation Engineers (SPIE) Conference Series*, Vol. 3356, *Society of Photo-Optical Instrumentation Engineers (SPIE) Conference Series*, ed. P. Y. Bely & J. B. Breckinridge, 234–248
- Galametz, A., Stern, D., Eisenhardt, P. R. M., et al. 2009, *ApJ*, 694, 1309
- Girardi, L., Bressan, A., Chiosi, C., Bertelli, G., & Nasi, E. 1996, *A&AS*, 117, 113
- Gómez, P. L., Nichol, R. C., Miller, C. J., et al. 2003, *ApJ*, 584, 210
- Häußler, B., Barden, M., Bamford, S. P., & Rojas, A. 2011, in *Astronomical Society of the Pacific Conference Series*, Vol. 442, *Astronomical Data Analysis Software and Systems XX*, ed. I. N. Evans, A. Accomazzi, D. J. Mink, & A. H. Rots, 155
- Hilton, M., Lloyd-Davies, E., Stanford, S. A., et al. 2010, *ApJ*, 718, 133
- Holtzman, J. A., Hester, J. J., Casertano, S., et al. 1995, *PASP*, 107, 156
- Hopkins, P. F., Hernquist, L., Cox, T. J., Dutta, S. N., & Rothberg, B. 2008, *ApJ*, 679, 156
- Hopkins, P. F., Hernquist, L., Cox, T. J., Robertson, B., & Springel, V. 2006, *ApJS*, 163, 50
- Jannuzi, B. T., & Dey, A. 1999, in *ASP Conf. Ser.*, Vol. 191, *Photometric Redshifts and the Detection of High Redshift Galaxies*, ed. R. Weymann, L. Storrie-Lombardi, M. Sawicki, & R. Brunner (San Francisco, CA: ASP), 111
- Jee, M. J., Rosati, P., Ford, H. C., et al. 2009, *ApJ*, 704, 672
- Jee, M. J., Dawson, K. S., Hoekstra, H., et al. 2011, *ApJ*, 737, 59
- Kaviraj, S., Cohen, S., Ellis, R. S., et al. 2013, *MNRAS*, 428, 925
- Kelson, D. D., & Holden, B. P. 2010, *ApJ*, 713, L28
- Kereš, D., Katz, N., Weinberg, D. H., & Davé, R. 2005, *MNRAS*, 363, 2
- Kimble, R. A., MacKenty, J. W., O’Connell, R. W., & Townsend, J. A. 2008, in *SPIE Conf. Ser.* 70101E, Vol. 7010
- Kodama, T. 1999, in *Astronomical Society of the Pacific Conference Series*, Vol. 163, *Star Formation in Early Type Galaxies*, ed. P. Carral & J. Cepa, 250
- Komatsu, E., Smith, K. M., Dunkley, J., et al. 2011, *ApJS*, 192, 18
- Kriek, M., van Dokkum, P. G., Labbé, I., et al. 2009, *ApJ*, 700, 221
- Kroupa, P. 2001, *MNRAS*, 322, 231
- Le Borgne, J.-F., Bruzual, G., Pelló, R., et al. 2003, *A&A*, 402, 433
- Lilly, S. J., Le Fèvre, O., Renzini, A., et al. 2007, *ApJS*, 172, 70
- Lilly, S. J., Le Brun, V., Maier, C., et al. 2009, *ApJS*, 184, 218
- Lotz, J. M., Primack, J., & Madau, P. 2004, *AJ*, 128, 163
- Magnelli, B., Elbaz, D., Chary, R. R., et al. 2009, *A&A*, 496, 57
- Mancone, C. L., Gonzalez, A. H., Brodwin, M., et al. 2010, *ApJ*, 720, 284
- Mancone, C. L., Baker, T., Gonzalez, A. H., et al. 2012, *ApJ*, 761, 141
- Marcillac, D., Elbaz, D., Chary, R. R., et al. 2006, *A&A*, 451, 57
- Martini, P., Miller, E. D., Brodwin, M., et al. 2013, *ApJ*, 768, 1
- McCracken, H. J., Milvang-Jensen, B., Dunlop, J., et al. 2012, *A&A*, 544, 156
- Mei, S., Holden, B. P., Blakeslee, J. P., et al. 2006, *ApJ*, 644, 759
- , 2009, *ApJ*, 690, 42
- Mei, S., Stanford, S. A., Holden, B. P., et al. 2012, *ApJ*, 754, 141
- Moustakas, J., Coil, A. L., Aird, J., et al. 2013, *ApJ*, 767, 50
- Murphy, E. J., Chary, R.-R., Alexander, D. M., et al. 2009, *ApJ*, 698, 1380
- Murphy, E. J., Condon, J. J., Schinnerer, E., et al. 2011, *ApJ*, 737, 67
- Murray, S. S., Kenter, A., Forman, W. R., et al. 2005, *ApJS*, 161, 1
- Muzzin, A., Wilson, G., Lacy, M., Yee, H. K. C., & Stanford, S. A. 2008, *ApJ*, 686, 966
- Muzzin, A., Marchesini, D., Stefanon, M., et al. 2013, *ApJS*, 206, 8
- Naab, T., & Burkert, A. 2003, *ApJ*, 597, 893
- Negroponte, J., & White, S. D. M. 1983, *MNRAS*, 205, 1009
- Nordon, R., Lutz, D., Shao, L., et al. 2010, *A&A*, 518, L24
- Oemler, A. 1974, *ApJ*, 194, 1
- Peng, C. Y., Ho, L. C., Impey, C. D., & Rix, H.-W. 2010, *AJ*, 139, 2097
- Polletta, M., Tajer, M., Maraschi, L., et al. 2007, *ApJ*, 663, 81
- Rieke, G. H., Young, E. T., Engelbracht, C. W., et al. 2004, *ApJS*, 154, 25
- Rines, K., & Diaferio, A. 2006, *AJ*, 132, 1275
- Rodighiero, G., Cimatti, A., Gruppioni, C., et al. 2010, *A&A*, 518, L25
- Rosati, P., Tozzi, P., Gobat, R., et al. 2009, *A&A*, 508, 583
- Saintonge, A., Tran, K.-V. H., & Holden, B. P. 2008, *ApJ*, 685, L113
- Sanders, D. B., Soifer, B. T., Elias, J. H., et al. 1988, *ApJ*, 325, 74
- Santos, J. S., Altieri, B., Popesso, P., et al. 2013, *MNRAS*, 433, 1287
- Scoville, N., Aussel, H., Brusa, M., et al. 2007, *ApJS*, 172, 1
- Snyder, G. F., Brodwin, M., Mancone, C. M., et al. 2012, *ApJ*, 756, 114
- Springel, V., White, S. D. M., Jenkins, A., et al. 2005, *Nature*, 435, 629
- Stanford, S. A., Eisenhardt, P. R., & Dickinson, M. 1998, *ApJ*, 492, 461
- Stern, D., Eisenhardt, P., Gorjian, V., et al. 2005, *ApJ*, 631, 163
- Strazzullo, V., Rosati, P., Pannella, M., et al. 2010, *A&A*, 524, A17
- Swinyard, B. M., Ade, P., Baluteau, J.-P., et al. 2010, *A&A*, 518, L4
- Tran, K.-V. H., Papovich, C., Saintonge, A., et al. 2010, *ApJ*, 719, L126
- Utomo, D., Kriek, M., Labbé, I., Conroy, C., & Fumagalli, M. 2014, *ApJ*, 783, L30
- Webb, T. M. A., O’Donnell, D., Yee, H. K. C., et al. 2013, *AJ*, 146, 84
- Wylezalek, D., Vernet, J., De Breuck, C., et al. 2014, *ApJ*, 786, 17
- Zeimann, G. R., Stanford, S. A., Brodwin, M., et al. 2013, *ApJ*, 779, 137